

Large magnetically induced strains in $\text{Ni}_{50}\text{Mn}_{28.7}\text{Ga}_{21.3}$ driven with collinear field and stress

A. Malla and M. J. Dapino^{a)}*Department of Mechanical Engineering, The Ohio State University, Columbus, Ohio 43202*

T. A. Lograsso and D. L. Schlagel

Ames Laboratory, U.S. Department of Energy, Ames, Iowa 50011

(Received 18 July 2005; accepted 26 January 2006; published online 20 March 2006)

Despite the huge magnetic-field-induced strain (MFIS) of up to 9.5% exhibited by certain Ni–Mn–Ga alloys, their usefulness in applications is severely hindered by the electromagnet device needed for driving the alloys with a magnetic field and orthogonal loading stress. In this paper we present macroscopic measurements obtained from a single crystal of $\text{Ni}_{50}\text{Mn}_{28.7}\text{Ga}_{21.3}$ which demonstrate a large reversible MFIS of -4100 ppm when the alloy is driven with quasistatic magnetic fields and fixed compressive stresses applied collinearly along the $[001]$ axis. This collinear configuration marks a fundamental difference with prior research in the field and points to the existence in this alloy of stable bias or residual stresses—likely associated with pinning sites in the alloy—which provide the energy necessary to restore the original variant state when the field is reversed. We present macroscopic magnetomechanical measurements which show a decrease of the MFIS with increasing stress loading and a stiffening of the alloy with increasing dc fields. The latter behavior is phenomenologically similar to the ΔE effect in magnetostrictive materials. The large reversible MFIS and tunable stiffness properties exhibited by this alloy could enable practical Ni–Mn–Ga actuators for high-deflection, low-force applications which due to being driven by a solenoid transducer are more compact, energy efficient, and faster than their electromagnet counterpart. A thermodynamic model is presented which qualitatively characterizes the decay in MFIS with increasing compressive external load and provides a starting point for the characterization, design, and control of the proposed Ni–Mn–Ga devices. © 2006 American Institute of Physics.

[DOI: [10.1063/1.2177927](https://doi.org/10.1063/1.2177927)]

I. INTRODUCTION

Ferromagnetic shape memory (FSM) refers to the reversible deformations exhibited by a martensitic material caused by either martensitic variant reorientation or austenite to martensite transformation in response to magnetic fields. In the Heusler alloy Ni_2MnGa , cooling below the characteristic martensite start temperature M_s produces a cubic to tetragonal transformation and a corresponding twin-variant structure. Over a certain compositional range, a typical martensite microstructure consists of a mixture of three variants, each with tetragonal lattice $c \times c \times a$ ($c/a=0.94$), in which adjacent variants are separated by a boundary known as a twin plane.¹ Large magnetic-field-induced strain (MFIS) results from the reorientation of favorable martensite variants through the motion of twin boundaries. Extensional room-temperature strains of 6% have been reported by Murray *et al.*² The largest FSM deformations to date, of about 9.5%, have been obtained in orthorhombic seven-layered alloys.³

In Ni–Mn–Ga, the pseudoelasticity associated with the reorientation of twin variants takes place solely in the low-temperature martensitic phase and is driven by magnetic fields or stresses. Since both magnetic fields and compressive stresses favor alignment of the short c axis of the tetragonal

unit cell, a fixed stress or magnetic field oriented perpendicular to the drive field must be applied to restore the twin variants and obtain reversible MFIS when the drive field is cycled. In applications, this is often done by placing a rectangular alloy in an electromagnet with the drive field applied along the $[110]$ direction and the load axis oriented along the $[001]$ direction—both directions relative to the parent austenite phase. This perpendicular configuration is shown in Fig. 1(a). Electromagnets tend to be bulky and heavy in addition to having low energy density due to the high reluctance of the air gap and low frequency bandwidth due to large eddy current losses. This implies that despite the huge strain potential of Ni–Mn–Ga, practical actuators and sensors based on these alloys are unfeasible due to the performance constraints imposed by electromagnets.

We are interested in the MFIS of Ni–Mn–Ga along the $[001]$ direction with fields applied along the same direction. This *collinear* configuration presents the critical advantage that it allows to drive the alloy with a solenoid transducer like that shown in Fig. 1(b). This transducer architecture includes a path for flux return and is thus significantly more compact, lightweight, and energy efficient than its electromagnet counterpart. Despite the apparent absence of a mechanism in the collinear configuration to restore the variant structure upon reversal of the field, experimental results have been published which show that moderate reversible deformations are possible in Ni–Mn–Ga driven in this man-

^{a)}Author to whom correspondence should be addressed; electronic mail: dapino.1@osu.edu

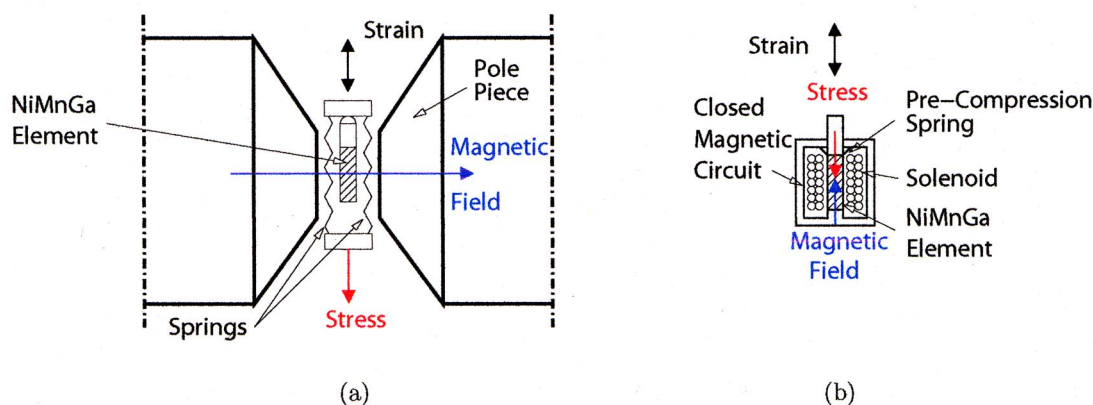


FIG. 1. (Color online) (a) Conventional electromagnet apparatus (partial view excluding coil and the rest of C core). (b) Solenoid transducer design and corresponding collinear field-stress drive configuration.

ner. These results point to additional strain mechanisms not fully accounted for by existing theory.

Wu *et al.*⁴ have reported a large recoverable MFIS of -3100 ppm in the $[001]$ direction of an off-stoichiometry single crystal of $\text{Ni}_{52}\text{Mn}_{22.2}\text{Ga}_{25.8}$ driven by a 20 kOe field along the $[001]$ direction. This alloy showed a martensitic self-strain of 2% , about a hundred times as large as that of Ni_2MnGa , thus suggesting that the martensite variants in a large fraction of the alloy are preferentially oriented. This reduces the degree of self-accommodation and leads to reduced deformations compared with the 6% strains achievable by reorientation of the c axis throughout the alloy. The measured deformations are very significant, nonetheless, as they compare favorably with those of Terfenol-D. However, the combination of high fields and low martensitic transformation temperature, which in this alloy is situated slightly below room temperature, precludes the practical implementation of this alloy in motion generation systems. Ohmic and eddy current heating produced within the solenoid transducer would easily cause the alloy to transform to its austenitic phase.

In this paper, we report large reversible strains of -4100 ppm along the $[001]$ direction of a cylindrical $\text{Ni}_{50}\text{Mn}_{28.7}\text{Ga}_{21.3}$ single-crystal rod driven with a sinusoidal magnetic field applied along the same direction and no external restoring force. We also present strain versus magnetic field curves obtained under varied compressive stresses applied along the field direction. These magnetomechanical tests are complemented by strain versus stress curves measured under varied dc bias fields, which are used to establish the dependence of elastic modulus with stress and field. The results show a stiffening of the alloy with increasing dc fields in a manner which is phenomenologically similar to the ΔE effect in rare-earth-iron compounds.⁵ The measurements were performed at room temperature on the alloy as cast, that is, without thermal, magnetic, or stress treatments. While in the experiments by Wu *et al.*⁴ repeated cycling of the field was necessary to achieve repeatable strains, the MFIS exhibited by our sample has remained invariant despite exposure of the alloy to a large number of field and stress cycles. These unexpected results cannot be explained by the current models for twin-variant reorientation in Ni–Mn–Ga–based

on the competing effects of the stress energy and Zeeman energy as the latter attempts to overcome the twin boundary energy—and point to the existence of bias or residual stresses built in the alloy during the crystal growth. We propose that the bias stresses stem from pinning sites or point defects in the alloy which act as localized energy potentials that oppose twin boundary motion and provide an otherwise nonexistent restoring force when the magnetic field is removed. The presence of pinning sites also explains the reduced deformations relative to alloys capable of over 6% strain, in which twin boundary is largely unimpeded as illustrated in the top panel of Fig. 2.

A recent study has shown that Ni–Mn–Ga alloys are extremely susceptible to impurities; sulfide and tantalum inclusions, and titanium-rich precipitates have been observed.⁶ It was assumed that for the large, incoherent S and Ta inclusions observed, dislocations would have to loop around the impurities in order for twin boundary motion to occur. Since the observed Ti precipitates are much smaller than the S and Ta inclusions, it was argued that the mechanism of dislocation motion in the presence of Ti precipitates is most likely cutting through the particles, as opposed to looping. By cutting, the dislocations form two new interfaces which provide a low-energy path for dislocation movement as compared to looping around the particles. It was estimated that the small Ti-rich precipitates have a strength of approximately $0.53 K_m$, thus acting as pinning sites which could be overcome by the application of sufficiently large magnetic fields. These small precipitates do not seem to impact the MFIS of the alloys studied as strains of 6% were observed.

We hypothesize that low-energy pinning sites do not contribute to the mechanism for reversible MFIS in the alloy investigated; during the first few field cycles after manufacture of the alloy, the twin boundaries have unattached from these sites and permanently attached to higher-energy sites. Hence, the twin boundaries are normally pinned to point defects whose energy is greater than the anisotropy energy. When a small magnetic field is applied along the $[001]$ direction, the twin boundaries attempt to displace according to the standard mechanisms for twin-variant reorientation, but the Zeeman energy that drives the motion of the twin boundaries is insufficient to completely overcome the energy po-

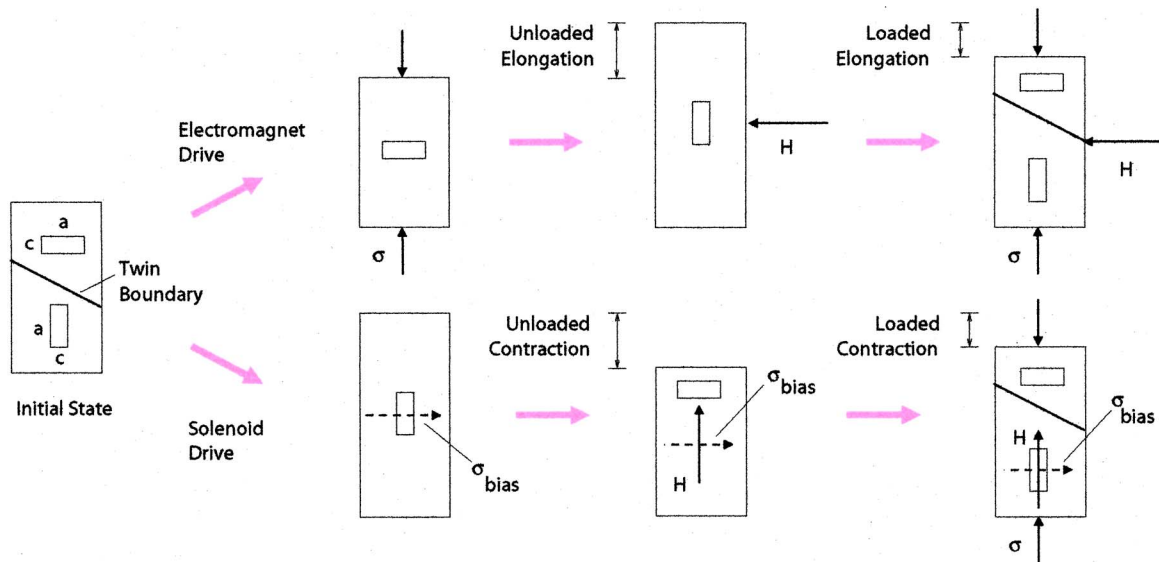


FIG. 2. (Color online) Schematic showing a two-variant system in an initial state (left); strain mechanism for Ni–Mn–Ga driven by an orthogonal stress-field pair (top panel); strain mechanism for Ni–Mn–Ga driven by a parallel stress-field pair (bottom panel). The magnetic field is denoted H , the external stress load is denoted σ , and the internal bias stress produced by pinning sites is denoted σ_{bias} .

tential of the pinning sites. Instead, the twin boundaries loop around the impurities and as they do work against the pinning sites, energy is dissipated. Saturation is achieved when the Zeeman energy is large enough to overcome the anisotropy energy and the magnetic moments become aligned with the field without changing the orientation of the crystal. When the field is removed, the anisotropy energy returns the magnetic moments to the easy c axis of the crystal and the pinning site energy provides a restoring mechanism for the twin boundaries, returning the sample to its original length and magnetization value. The pinning energy can thus be interpreted as an internal bias stress field oriented perpendicular to the $[001]$ direction, as shown in the bottom panel of Fig. 2. The internal bias stress can thus be approximated as the applied stress for which twin boundary mobility is zero. This also implies that excessive pinning energy will render the alloy inactive as the available Zeeman pressure is insufficient to drive the motion of twin boundaries away from the pinning sites.

II. EXPERIMENTS

A. Material preparation

A nonstoichiometric Ni–Mn–Ga rod measuring 6.35 mm in diameter by 22.43 mm in length with chemical composition (wt %) $\text{Ni}_{50}\text{Mn}_{28.7}\text{Ga}_{21.3}$ was used in the measurements presented here. The rod was prepared as follows: appropriate quantities of high purity nickel, manganese, and gallium were cleaned and arc-melted several times under an argon atmosphere. The buttons were remelted and the alloy drop cast into a chilled copper mold to ensure compositional homogeneity throughout the ingot. The crystal was grown from the as-cast ingot in an alumina Bridgman style crucible which was heated to 1350 °C under a pressure of 1.3×10^{-4} Pa to degas the crucible and charge. After melting, the chamber was backfilled to a pressure of 2.76×10^5 Pa with high purity argon to eliminate gas pockets and to mini-

mize the amount of manganese evaporation from the melt during the crystal growth. The ingot was held at 1350 °C for 1 h to allow thorough mixing before withdrawing the sample from the heat zone at a rate of 5 mm/h. The sample was cut from the crystal boule along the $[001]$ direction by electric discharge milling, and its composition measured along the longitudinal axis by energy dispersive microanalysis. The longitudinal direction of the rod thus coincides with the $[001]$ direction of the crystal. Thermomechanical properties of the alloy are summarized in Table I; x-ray diffraction tests show that the alloy's structure is tetragonal at room temperature.

B. Free-strain measurements

For the strain measurements the Ni–Mn–Ga rod was placed in a fixture which comprises a water-cooled solenoid and a load frame for application of compressive stresses parallel to the magnetic field direction. The solenoid is surrounded by a cylindrical housing and top and bottom plates which provide a close magnetic path for routing of the flux

TABLE I. Thermomechanical properties of the $\text{Ni}_{50}\text{Mn}_{28.7}\text{Ga}_{21.3}$ rod tested in this study. The transformation temperatures (austenite start A_s , austenite finish A_f , martensite start M_s , martensite finish M_f , and Curie temperature T_C) were measured at the top and bottom of the rod.

| Parameter | Value |
|----------------------|-----------------------------------|
| e/a (7Mn+10Ni+3Ga) | 7.648 |
| Length (mm) | 22.43 |
| Density (g/cc) | 7.886 |
| A_s | 42 °C (top), 43.7 °C (bottom) |
| A_f | 65.9 °C (top), 62.5 °C (bottom) |
| M_s | 55.3 °C (top), 54.8 °C (bottom) |
| M_f | 32.4 °C (top) 33.1 °C (bottom) |
| T_C (heating) | 101.1 °C (top), 100.6 °C (bottom) |
| T_C (cooling) | 98 °C (top), 98.2 °C (bottom) |

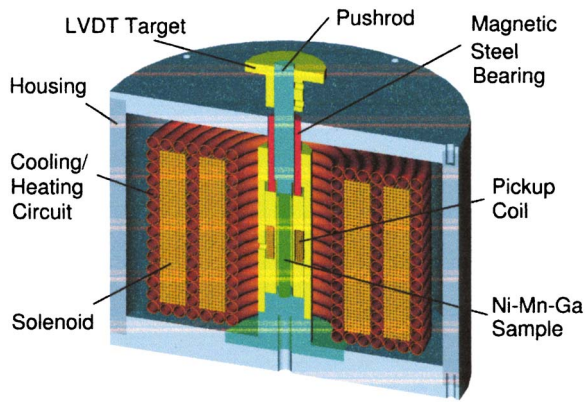


FIG. 3. (Color online) Schematic representation of the solenoid apparatus employed in this study.

into the rod (Fig. 3). The MFIS was measured with a linear variable differential transducer (LVDT) and strain gages. Since the sample is shorter than the height of the solenoid, AISI 1144 steel rods of equal length were waxed to the top and bottom of the sample, for both positioning the sample symmetrically at the center of the solenoid and aiding in the closing of the magnetic flux. Compressive loading was applied through an AISI 1144 pushrod which is connected to the loading cross bar with a nonmagnetic stainless steel rod for magnetic isolation between the solenoid and load frame. The pushrod slides in a precision linear bearing.

The alternating magnetic field had an amplitude of up to 725 kA/m and a frequency of 0.1 Hz. Mapping of the field along the length of the solenoid was conducted with a Hall sensor and through finite element calculations. Because Ni-Mn-Ga is mechanically soft, magnetic forces acting on the pushrod were quantified and their effect subtracted from the measured deformations in order to accurately quantify the MFIS produced by the $\text{Ni}_{50}\text{Mn}_{28.7}\text{Ga}_{21.3}$ rod. Furthermore, the magnetostriction of the steel components was quantified and correspondingly subtracted from the measured deformations.

The solid line in Fig. 4 shows the MFIS measured by a strain gage oriented parallel to the [001] direction with zero applied stress. A maximum compressive strain of -4100 ppm was obtained; the contraction of the rod is consistent with the rotation of the c axis toward the [001] direction. Independent confirmation of this result was conducted at Iowa State University⁷ (ISU) and Naval Surface Warfare Center (NSWC).⁸ The triangles in Fig. 4 show the ISU measurement, in which the $\text{Ni}_{50}\text{Mn}_{28.7}\text{Ga}_{21.3}$ rod was strain gaged and placed longitudinally between the poles of an electromagnet. Excellent agreement with our measurements is observed.

For the NSWC tests, the change in length of the rod under zero stress was measured. A static magnetic field of 560 kA/m was applied transverse to the rod direction and parallel to the rod direction by means of an electromagnet. The rod was located on a pole face and kept in place by a styrofoam holder. The length of the rod was measured with a caliper at zero field after application of a transverse field and subsequently at zero field after application of a longitudinal field. The measured fractional change of length is

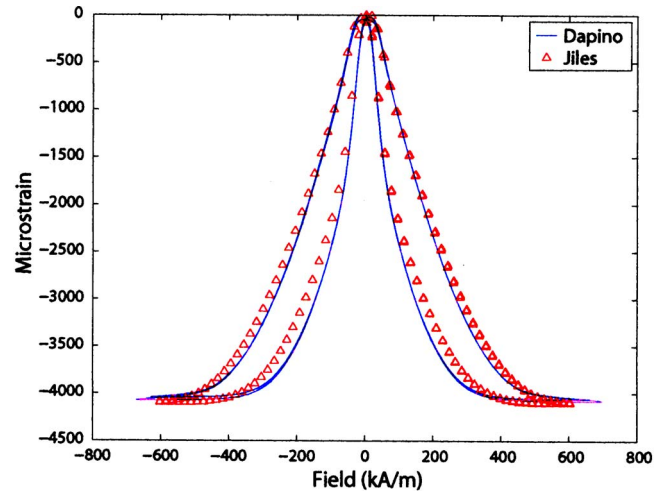


FIG. 4. (Color online) Solid line: MFIS measured in the [001] direction as a function of the magnetic field applied along the same direction. The triangles represent measurements conducted at Iowa State University on the same rod under similar conditions but employing an electromagnet.

-4000 ppm, which is consistent with our results since the applied field was lower than in our measurements.

C. Magnetomechanical tests

Strain versus field curves at various fixed compressive stresses are shown in Fig. 5. The stresses were applied by means of dead weights for a total stress range of 0–58.23 MPa. For clarity, the measurements are shown in two panels, (a) and (b), which, respectively, show the ranges of 0.13–5.63 MPa and 7.03–19.69 MPa. Since both the external stress and applied magnetic field favor alignment of the variants with the c axis aligned along the longitudinal rod axis, the volume available for reorientation of variants by magnetic field and associated MFIS decrease with increasing external stress. Further, the MFIS beyond a certain stress limit becomes negligible and only magnetostriction is present. This behavior is illustrated for the complete range of stresses investigated in Fig. 6, where the abscissa represents the maximum MFIS obtained at a given stress value. Over this range of stresses, the maximum MFIS becomes stable at approximately -150 ppm for compressions greater than 19 MPa.

Compression cycles conducted at various static magnetic fields ranging between 0 and 378 kA/m are shown in Fig. 7. Each curve was obtained by applying a constant magnetic field and subsequently applying a cyclic compressive stress with amplitude of 13.36 MPa. Each curve is thus shifted relative to the line of zero strain by an amount equal to the compressive MFIS produced by the given magnetic field. After completion of a given compression cycle, the field was incremented to the value used on the next compression cycle without resetting the strain. Figure 7 reflects the nonlinear and hysteretic dependence between stress and strain for this alloy. The amount of hysteresis decreases with increasing field and a saturation effect is observed since as the field is increased, the available MFIS decreases as the volume of variants available for reorientation decreases. Nonclosure of the cycles is observed which is due to the remanent magne-

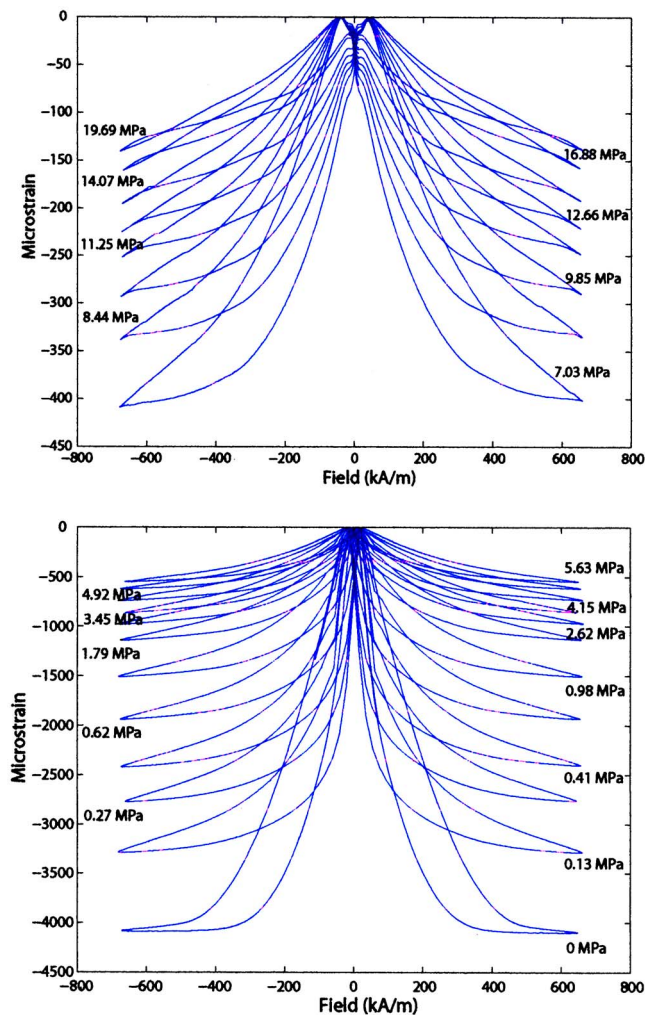


FIG. 5. (Color online) Strain vs magnetic field as a function of stress: range of 0–5.63 MPa (bottom) and range of 7.03–19.69 MPa (top).

tization producing a certain amount of compression after removal of the field. The nonclosure decreases with increasing static field.

The data also suggest a strong magnetoelastic coupling which phenomenologically behaves closer to the coupling in

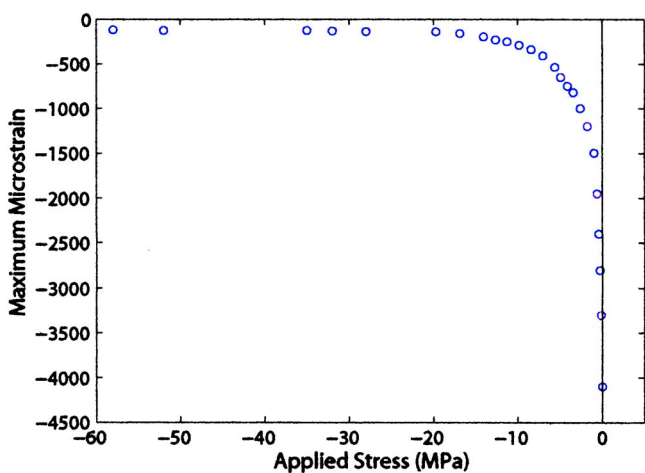


FIG. 6. (Color online) Maximum MFIS vs applied stress.

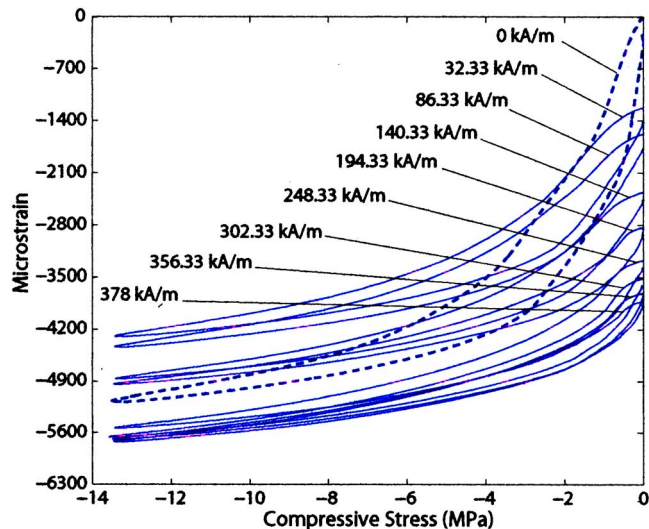


FIG. 7. (Color online) Strain-stress cycles at different static field values. After completion of a given compression cycle, the field was incremented to the value used on the next compression cycle without resetting the strain.

Terfenol-D (Ref. 9) than that associated with shape memory and magnetic pseudoelasticity.¹⁰ To further illustrate this coupling, we show in Fig. 8 data extracted from Fig. 7 where for clarity only the loading portion of the compression cycles is shown, the strain offsets have been removed, and the abscissa and ordinate have been swapped. These curves suggest an overall stiffening with increasing dc field, consistent with the field-induced stiffening measured dynamically by Faidley *et al.*¹¹ As a bias magnetic field is applied, the stiffer variants with the short c axis aligned with the field are favored and grow by twin boundary motion. Since in Ni–Mn–Ga the magnetization of the unit cell is rigidly attached to the c axis, this selective alignment biases the initial magnetization towards the saturated state and produces a decrease in the MFIS possible by twin boundary motion. Cullity¹² has shown that the amount of additional strain beyond the elastic strain is directly related to the decrease in elastic modulus from that of the material when only elastic strain is possible, often referred to as the ΔE effect. To illustrate this effect in

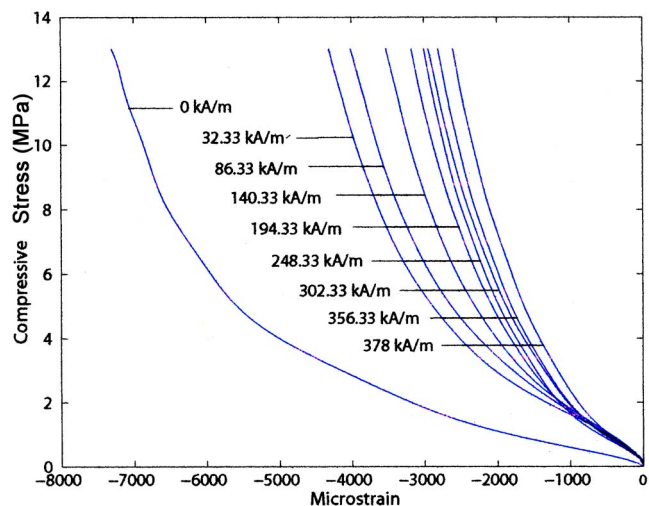


FIG. 8. (Color online) Loading curves at different dc magnetic field values.

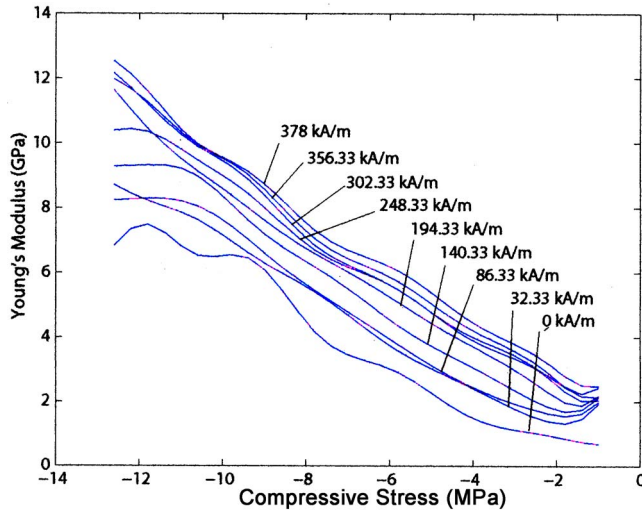


FIG. 9. (Color online) Variation in elastic modulus with compressive stress at different dc field values.

Ni-Mn-Ga driven with a collinear field and stress, the dependence of the elastic modulus with stress and field, calculated from Fig. 8, is shown in Figs. 9 and 10, respectively.

D. Magnetization measurements

The magnetization was measured with a pickup coil wound on an aluminum spool which surrounds the Ni-Mn-Ga rod. Saturation magnetization was measured at 381 kA/m. The coercive field is very low at about 8.8 kA/m, while the remanent magnetization has a value of 183 kA/m, corresponding to 0.23 T. For stresses up to 58 MPa, the magnetization curve is observed to not change as a function of stress.

III. THEORY

We are interested in characterizing the MFIS as a function of magnetic fields and applied stresses. To that end, we

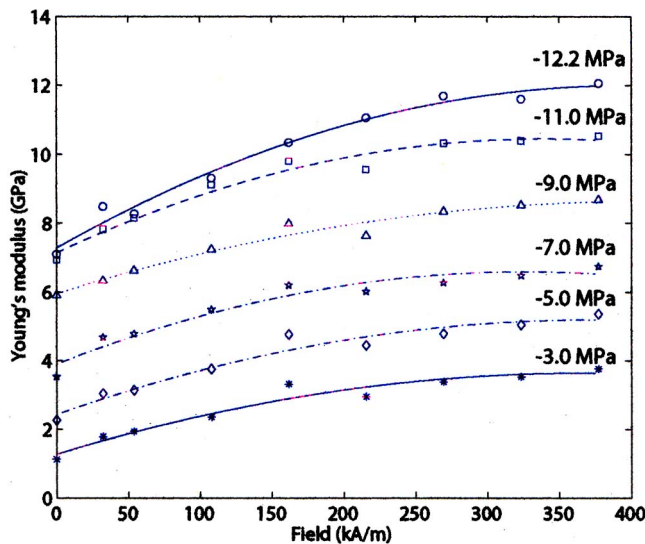


FIG. 10. (Color online) Variation in elastic modulus with dc magnetic field at different compressive stresses. The markers indicate the measured data while the lines are polynomial fits to the data.

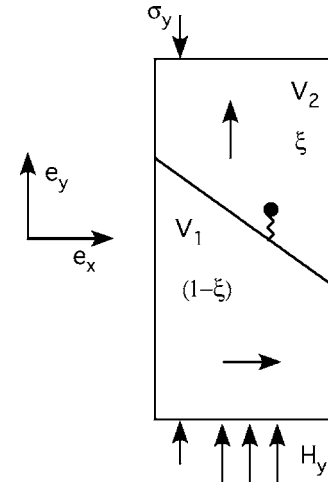


FIG. 11. Twin martensite variants in a Ni-Mn-Ga alloy subjected to collinear magnetic fields H_y and stresses σ_y .

consider a simplified two-variant system, shown in Fig. 11, and the corresponding Gibbs free energy which is written as a function of the Zeeman energy difference between the variants, the stress energy and the energy of the boundary. Variant 2 has a volume fraction of ξ and is that which has the c axis aligned with the axial magnetic field H_y . Variant 1 is the transverse variant with magnetization vectors oriented in the c axis and has a volume fraction of $(1-\xi)$. This construct has been detailed by Faidley *et al.*¹³ on the basis of thermodynamic considerations in the manner of Kiefer and Lagoudas^{14,15} and Hirsinger and Lexcellent.¹⁶ The system can thus be treated as a mixture of variants with scalar free energy,

$$G(\sigma_y, H_y, T) = (1 - \xi)G^1 + \xi G^2 + G^b, \quad (1)$$

where G^i is the energy of the i th variant and G^b is the energy of the boundary between the two variants. In order to write expressions for G^i , it is assumed that (a) the system is isothermal and (b) the fields are large enough to ensure that the effects of the magnetic domains can be ignored. In this case the expression for the energy of each variant is given by a standard expression for the Gibbs free energy,¹⁷

$$G^i(\sigma_y, H_y) = \psi^i - \frac{1}{2\rho} \sigma_y S_{yy}^i \sigma_y - \frac{\mu_0}{\rho} M^i H_y, \quad (2)$$

where ψ^i , S_{yy}^i , and M^i , respectively, denote the Helmholtz energy, mechanical compliance, and magnetization of the i th variant, σ_y is the applied stress, ρ is the density, and μ_0 is the permeability of free space. The Gibbs free energy of each variant is equal to the Helmholtz energy minus the elastic and Zeeman energies.

The energy of the twin boundary stems from two sources. The first is the energy necessary to rotate a unit cell, which can be expressed as work done to overcome a force; the second is the energy of the pinning sites, which can be modeled as that of a mechanical spring. Thus the boundary energy term has the form

$$G^b = \begin{cases} c_1\xi + k_1\xi^2, & \dot{\xi} > 0 \\ c_2\xi + k_2\xi^2, & \dot{\xi} < 0, \end{cases} \quad (3)$$

where k_i ($i=1,2$) is the effective spring constant of the pinning sites, c_i ($i=1,2$) is the force associated with cell reorientation, and the two branches of the function occur because the material behavior is not the same when the field is increasing and variant 2 is growing as it is when the field is decreasing and variant 2 is shrinking.

Substitution of (2) and (3) into (1) yields

$$G(\sigma_y, H_y) = \psi^j - \frac{1}{2\rho} S_{yy}^1 \sigma_y^2 + \xi \left[-\frac{1}{2\rho} \Delta S_{yy} \sigma_y^2 - \frac{\mu_0 M_s}{\rho} H_y \right] + \begin{cases} c_1\xi + k_1\xi^2, & \dot{\xi} > 0 \\ c_2\xi + k_2\xi^2, & \dot{\xi} < 0, \end{cases} \quad (4)$$

where the Δ operator refers to the difference between the two variants and $\Delta\psi=0$ since the Helmholtz energies of the two variants are identical. To establish a condition for the onset of twin-variant motion, we consider a thermodynamic driving force π^ξ as proposed for ferromagnetic shape memory materials by Kiefer and Lagoudas,¹⁴

$$\pi^\xi = \epsilon_s \sigma_y - \rho \frac{\partial G}{\partial \xi}, \quad (5)$$

where ϵ_s is the saturation strain. The condition is obtained by considering the energy balance between the thermodynamic force driving the motion of the twin boundary and the energy dissipated during the motion,

$$\pi^\xi = \pm Y^\xi, \quad (6)$$

with Y^ξ a positive quantity representing the dissipation of energy. The plus sign represents the reorientation of variant 2 into variant 1 and the minus sign represents the opposite case.

Differentiation of (4) and substitution into (5) yields the force balance

$$\pm Y^\xi = \epsilon_s \sigma_y - \frac{1}{2} \Delta S_{yy} \sigma_y^2 - \mu_0 M_s H_y - \rho \begin{cases} c_1 + 2k_1\xi, & \dot{\xi} > 0 \\ c_2 + 2k_2\xi, & \dot{\xi} < 0. \end{cases} \quad (7)$$

Expression (7) can then be solved for the volume fraction,

$$\xi = \begin{cases} 1/(2\rho k_1) (\epsilon_s \sigma_y + \frac{1}{2} \Delta S_{yy} \sigma_y^2 + \mu_0 M_s H_y - \rho c_1 - Y^\xi), & \dot{\xi} > 0 \\ 1/(2\rho k_2) (\epsilon_s \sigma_y + \frac{1}{2} \Delta S_{yy} \sigma_y^2 + \mu_0 M_s H_y - \rho c_2 + Y^\xi), & \dot{\xi} < 0, \end{cases} \quad (8)$$

which is dependent on the applied field H_y and axial stress σ_y . To facilitate the numerical implementation, expression (8) is rewritten as

$$\xi = \begin{cases} A_1 (\epsilon_s \sigma_y + \frac{1}{2} \Delta S_{yy} \sigma_y^2 + \mu_0 M_s H_y - \rho c_1 - Y^\xi), & \dot{H} > 0 \text{ and } \xi < \xi_s \\ \xi_s, & \xi > \xi_s \\ A_2 (\epsilon_s \sigma_y + \frac{1}{2} \Delta S_{yy} \sigma_y^2 + \mu_0 M_s H_y - \rho c_2 + Y^\xi), & \dot{H} < 0 \text{ and } \xi < \xi_s, \end{cases} \quad (9)$$

where $A_1 = 1/(2\rho k_1)$, $A_2 = 1/(2\rho k_2)$, and ξ_s is the saturation volume fraction. The strain is related to the volume fraction by

$$\epsilon = \xi \epsilon_{th}, \quad (10)$$

with ϵ_{th} the maximum theoretical strain which would occur if a single boundary swept through the entire material, hence producing a change in ξ from 0 to 1. Hence, for the case where the twin boundaries are restrained by pinning sites, ξ will be limited to a much smaller range.

Parameters that need to be identified in this model include k_1 , k_2 , ϵ_s , ΔS_{yy} , M_s , c_1 , c_2 , and Y^ξ . Parameters ΔS_{yy} , M_s , and Y^ξ were obtained from published data.¹⁴ The remaining parameters were determined phenomenologically by fitting of strain versus magnetic field data at a particular applied stress σ_p . As shown in Fig. 12, three data points provide the following information: (i) field H_1 at the strain turn around point, (ii) strain ϵ_2 at the crossover point, (iii) field H_3 at the onset of saturation, and (iv) saturation strain

ϵ_s . Using these measurements, the equations in Table II can be used to calculate the parameters needed to implement relations (9) and (10).¹³ Model results for various compressive

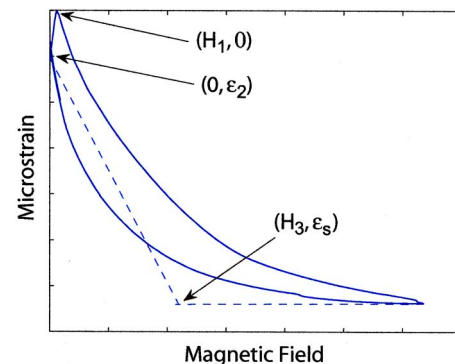


FIG. 12. (Color online) Data points used for identification of model parameters.

TABLE II. Summary of model parameters employed in Fig. 13.

| |
|--|
| $\Delta S_{yy}=0$ |
| $M_s=0.622 \text{ MA/m}$ |
| $Y^\xi=0.2 \times 10^6 \text{ J}$ |
| $\epsilon_{th}=-0.06$ |
| $k_1=1.5 k_2$ |
| $k_2=\frac{\mu_0 M_s H_3 \epsilon_{th}}{2(\epsilon_s - \epsilon_2)}$ |
| $c_1=\epsilon_s \sigma_p + \frac{1}{2} \Delta S_{yy} \sigma_p^2 + \mu_0 M_s H_1 - Y^\xi$ |
| $c_2=\epsilon_s \sigma_p + \frac{1}{2} \Delta S_{yy} \sigma_p^2 + Y^\xi - 2k_2 \frac{\epsilon_2}{\epsilon_{th}}$ |

strains are shown in Fig. 13, where it is noted that the model adequately characterizes the decay in maximum MFIS with increasing external load. Table II shows the model parameters employed in Fig. 13; further details regarding the numerical implementation of the model are given by Faidley *et al.*¹³

IV. DISCUSSION

This paper presents macroscopic measurements on the magnetomechanical behavior of a single crystal of $\text{Ni}_{50}\text{Mn}_{28.7}\text{Ga}_{21.3}$ driven with alternating magnetic fields and fixed compressive stresses applied along the [001] axis. This collinear field-stress drive configuration marks a fundamental difference with prior research on Ni–Mn–Ga alloys, which is largely based on orthogonal field-stress or field-field configurations in accordance with current theory for martensite variant reorientation. According to theory, reversible MFIS would not be possible in Ni–Mn–Ga driven in the manner examined in this investigation since both the magnetic field and stress favor the same variant. The measurements therefore point to an internal source of energy which

restores the original variant state upon reversal of the field direction. Since the reversible responses were measured on the alloy as cast and they have persisted after a large number of field and stress cycles, the internal restoring energy is attributed to high-energy pinning sites formed during manufacture of the alloy. The twin boundaries remain attached to high-energy pinning sites and loop around them under the action of magnetic fields or stresses.

The unloaded measurements show a large reversible MFIS of -4100 ppm . The measurements under increasing compressive stress indicate that in this alloy the maximum MFIS decays rapidly relative to the unloaded deformation and becomes stable at approximately -150 ppm for compressions greater than 19 MPa . The decay in MFIS is expected since mechanical loads collinear with the magnetic field promote the growth of variants with the c axis oriented with the field and reduce the volume available for reorientation of variants by magnetic field. Considering that the external stress and applied magnetic field promote looping of the twin boundaries around pinning sites and the internal bias stress opposes the looping, when the applied elastic and Zeeman energies equal the pinning energy—which in the presented model is assumed to be part of the boundary energy—the twin boundaries become immobilized and no more MFIS is possible. Beyond a certain stress limit the MFIS becomes negligible and only magnetostriction is present, as observed in Fig. 6. This stress limit provides a measure of the strength of the internal bias stress, but the exact determination of the internal bias stress requires knowledge of the initial configuration of variants in the alloy and how the configuration has been changed by the applied stress. In Fig. 7 the stress-strain curve at zero field is reversible even beyond the initial elastic region and when the alloy is in its quasiplastic region. This behavior is attributed to the internal bias stress which restores the initial configuration of the variants.

The ability of the studied alloy to do mechanical work against external loads is unsatisfactory for high-power actuator design, which is not unexpected since previous studies have shown that Ni–Mn–Ga alloys exhibit low blocking stresses.¹⁸ Notwithstanding, the strains of -4100 ppm represent over a twofold improvement over Terfenol-D, the most technologically advanced magnetostrictive material. This large MFIS could enable practical Ni–Mn–Ga actuators for high-deflection, low-force applications. It is emphasized that solenoid actuators are more compact, energy efficient, and faster than is possible to achieve through the conventional perpendicular field-stress drive configuration and mandatory electromagnet-based magnetic circuit. Furthermore, the ability to change the stiffness with dc fields can potentially lead to Ni–Mn–Ga tunable vibration absorbers and delay lines for underwater communications.

The model qualitatively characterizes the decay in MFIS with increasing compressive load. Because of its phenomenological nature, however, further work is needed for improving its physical fidelity and accuracy. To that end, further characterization by investigating the microstructural properties of the alloy will be necessary for determining the exact physical origin of the pinning sites. The formation of pinning sites during manufacture also hints at the possibility of de-

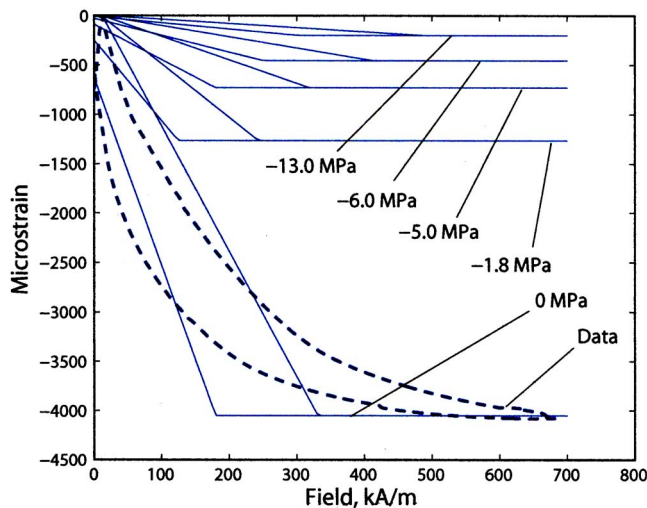


FIG. 13. (Color online) MFIS data and simulations illustrating the qualitative properties of the model.

veloping internal bias stresses by other methods, for example, stress annealing as done by Wun-Fogle *et al.*¹⁹ for Fe–Ge. Such methods could potentially yield deformations much larger than those found in the alloy investigated.

ACKNOWLEDGMENTS

Funding for two of the authors (A.M. and M.J.D.) was provided by The Ohio State University. The work of two of the authors (T.A.L. and D.L.S.) was supported by the Office of Basic Energy Sciences, Materials Sciences Division of the U.S. Department of Energy under Contract No. W-7405-ENG-82. The authors acknowledge LeAnn Faidley for her contribution on the development of the model.

¹R. Tickle, R. D. James, T. Shield, M. Wuttig, and V. V. Kokorin, *IEEE Trans. Magn.* **35**, 4301 (1999).

²S. J. Murray, M. Marioni, S. M. Allen, and R. C. O'Handley, *Appl. Phys. Lett.* **77**, 886 (2000).

³A. Sozinov, A. A. Likhachev, N. Lanska, and K. Ullakko, *Appl. Phys. Lett.* **80**, 1746 (2002).

⁴G. H. Wu *et al.*, *Appl. Phys. Lett.* **75**, 2990 (1999).

⁵A. E. Clark, in *Ferromagnetic Materials*, edited by E. P. Wohlfarth (North-Holland, Amsterdam, 1980), pp. 531–589.

⁶R. L. Richard, Ph.D. dissertation, Massachusetts Institute of Technology, 2005.

⁷D. C. Jiles (private communication).

⁸M. Wun-Fogle, J. Restorff, and A. E. Clark (private communication).

⁹R. Kellogg and A. Flatau, *J. Intell. Mater. Syst. Struct.* **15**, 117 (2004).

¹⁰R. N. Couch and I. Chopra, *Proc. SPIE* **5164**, 1 (2005).

¹¹L. E. Faidley, M. J. Dapino, and G. N. Washington, *J. Intell. Mater. Syst. Struct.* **117**, 123 (2006).

¹²R. D. Cullity, *Introduction to Magnetic Materials* (Addison-Wesley, Reading, MA, 1972).

¹³L. E. Faidley, M. J. Dapino, G. N. Washington, and T. A. Lograsso, *Proc. SPIE* **5761**, 501 (2005).

¹⁴B. Kiefer and D. C. Lagoudas, *Proc. SPIE* **5387**, 164 (2004).

¹⁵B. Kiefer and D. C. Lagoudas, *Philos. Mag.* **85**, 3871 (2005).

¹⁶L. Hirsinger and C. Lexcellent, *J. Magn. Magn. Mater.* **254–255**, 275 (2003).

¹⁷R. C. Smith, *Smart Material Systems: Model Development* (SIAM, Philadelphia, PA, 2005).

¹⁸R. Tickle and R. D. James, *J. Magn. Magn. Mater.* **195**, 627 (1999).

¹⁹M. Wun-Fogle, J. B. Restorff, and A. E. Clark, *Proc. SPIE* **5387**, 468 (2004).